Heterogeneous & Homogeneous & Bio- & Nano-

CHEM**CAT**CHEM

CATALYSIS

Accepted Article

Title: Size-dependent visible light photocatalytic performance of Cu2O nanocubes

Authors: Sekar Karthikeyan, Santosh Kumar, Lee J Durndell, Mark A Isaacs, Christopher M.A. Parlett, Ben Coulson, Richard Douthwaite, Zhi Jiang, Karen Wilson, and Adam Fraser Lee

This manuscript has been accepted after peer review and appears as an Accepted Article online prior to editing, proofing, and formal publication of the final Version of Record (VoR). This work is currently citable by using the Digital Object Identifier (DOI) given below. The VoR will be published online in Early View as soon as possible and may be different to this Accepted Article as a result of editing. Readers should obtain the VoR from the journal website shown below when it is published to ensure accuracy of information. The authors are responsible for the content of this Accepted Article.

A Journal of

ChemPubSoc
Europe

WILEY-VCH   www.chemcatchem.org

FULL PAPER

Size-dependent visible light photocatalytic performance of Cu₂O nanocubes

Sekar Karthikeyan,[a] Santosh Kumar,[b] Lee J. Durndell, [a] Mark. A. Isaacs, [a] Christopher M.A. Parlett,[a] Ben Coulson,[c] Richard E. Douthwaite,[c] Zhi Jiang,[d] Karen Wilson[e], and Adam F. Lee*[e]

Abstract: Well-defined Cu₂O nanocubes with tunable dimensions and physicochemical properties have been prepared using a simple one-pot reaction. Reduction of Cu(II) salts by ascorbic acid in the presence of PEG as a structure-directing agent affords crystalline Cu₂O nanocubes of between 50 to 500 nm. Optical band gap, band energies, charge-carrier lifetimes and surface oxidation state systematically evolve with nanocube size, and correlate well with visible light photocatalytic activity for aqueous phase phenol degradation and H₂ production which are both directly proportional to size (doubling between 50 and 500 nm). HPLC reveals fumaric acid as the primary organic product of phenol degradation, and selectivity increases with nanocube size at the expense of toxic catechol. Apparent quantum efficiencies reach 26 % for phenol photodegradation and 1.2 % for H₂ production using 500 nm Cu₂O cubes.

Introduction

Metal oxide based semiconductor photocatalysts are widely employed for environmental remediation[1] and solar fuels production via water splitting[2] and CO₂ reduction[3], due to their earth-abundance, low cost, and environmental sustainability.[4] Copper (I) oxide (Cu₂O) is an attractive semiconductor for large-scale applications such as wastewater treatment,[5] and possesses a narrow bandgap (2.0-2.2 eV) enabling visible light utilisation. In addition the position of the conduction band minimum (CBM) and valence band maximum (VBM) span the potentials for proton reduction and water oxidation required for overall water splitting.[6]. A wide range of Cu₂O morphologies are amenable to synthesis, including cubes,[7] rhombicuboctahedra,[8] polyhedra,[9] nanowires,[4] nanocages,[10] and hollow structures,[11] and consequently their facet-dependent photocatalytic properties have been investigated for the destruction of hazardous organic compounds.[12] However, few reports have explored particle size effects of copper oxides on photocatalytic performance, despite the well-known evolution of photophysical properties,[13] because the synthesis of well-defined Cu₂O nanostructures of tunable dimensions remains challenging.[14]

Wastewater depollution due to the unregulated discharge of recalcitrant organic compounds (ROCs), notably from textile, paper, drug, and food manufacturing, cannot be removed by conventional biological and/or physicochemical processing (e.g. microorganisms, flocculation or chlorination)[15] and represent a significant hazard for many developed and developing countries.[16] Such ROCs include toxic phenolics,[17] and their removal has been investigated using so-called advanced oxidation processes (AOPs) which utilise a range of highly oxidising species, either alone or in combination (e.g. O₃, O₃/H₂O₂, UV/O₃, UV/H₂O₂, O₃/UV/H₂O₂, and Fe²⁺/H₂O₂),[18] to decompose phenol in aqueous solution. Fenton-type AOPs which utilise the redox properties of certain transition metals, exhibit high removal efficiencies for diverse ROCs including phenols, but share a common requirement for H₂O₂ addition, and heterogeneous variants are susceptible to metal leaching.[19] Hence photocatalytic wastewater treatment, ideally employing visible light and O₂ (air), could offer a more cost-effective and sustainable alternative to current AOPs.

To date, various metal oxide nanostructures including TiO₂,[20] TiO₂/carbon,[21] metal/non-metal doped-TiO₂[22] and ZnO,[23] graphitic carbon nitride,[24] and Cu₂O composites[17] have been studied for phenol degradation, although quantitative comparisons between different photocatalysts is hampered by the lack of a standard testing protocol. Indeed, the majority of photocatalytic studies do not report either mass or surface area normalised rates. However, we recently reported that hierarchical Cu₂O nanocubes[5a] show high activity for methylene blue degradation (0.6 µmolg⁻¹min⁻¹ versus 0.008 µmolg⁻¹min⁻¹ for Cu₂O nanowires),[4] and a Cu₂O/TiO₂ p-n heterojunction photocatalyst has shown promise in aqueous phase p-nitrophenol degradation under artificial sunlight. Cu₂O is also an effective photocatalyst for H₂ evolution from water splitting,[2],[5a] with 300-500 nm Cu₂O nanocrystals exhibiting H₂ productivity of 0.16 µmolg⁻¹h⁻¹.[25] These compare to the composites 1 wt% MoS₂ /200-400 nm Cu₂O nanospheres[26] and 3 wt% Pt/Cu₂O-g-C₃N₄ nanocomposites giving 250 µmolg⁻¹h⁻¹,[27] although both studies used high power light sources (350 W and 300 W respectively) and sacrificial alcohol donors, and did not report quantum efficiencies. In contrast, we recently achieved 15 µmolg⁻¹h⁻¹ H₂, and an apparent

[a]   Dr. S. Karthikeyan, Dr. L. J. Durndell, Dr. C. M. A. Parlett, Dr. M. A. Isaacs
      European Bioenergy Research Institute
      Aston University
      Aston Triangle, Birmingham B4 7ET, UK
[b]   Dr. S. Kumar
      Department of Chemical Engineering
      University of Bath
      Bath BA2 7AY, UK
[c]   B. Coulson, Dr. R. E. Douthwaite
      Department of Chemistry
      University of York
      York YO10 5DD, UK
[d]   Dr Z. Jiang
      Research Center for Combustion and Environment Technology
      Shanghai Jiao Tong University
      Shanghai, P.R. China
[e]   Prof. A.F. Lee, Prof. K. Wilson
      School of Science
      RMIT University
      Melbourne VIC 3001, Australia
      E-mail: adam.lee2@rmit.edu.au

      Supporting information for this article is given via a link at the end of the document.

FULL PAPER
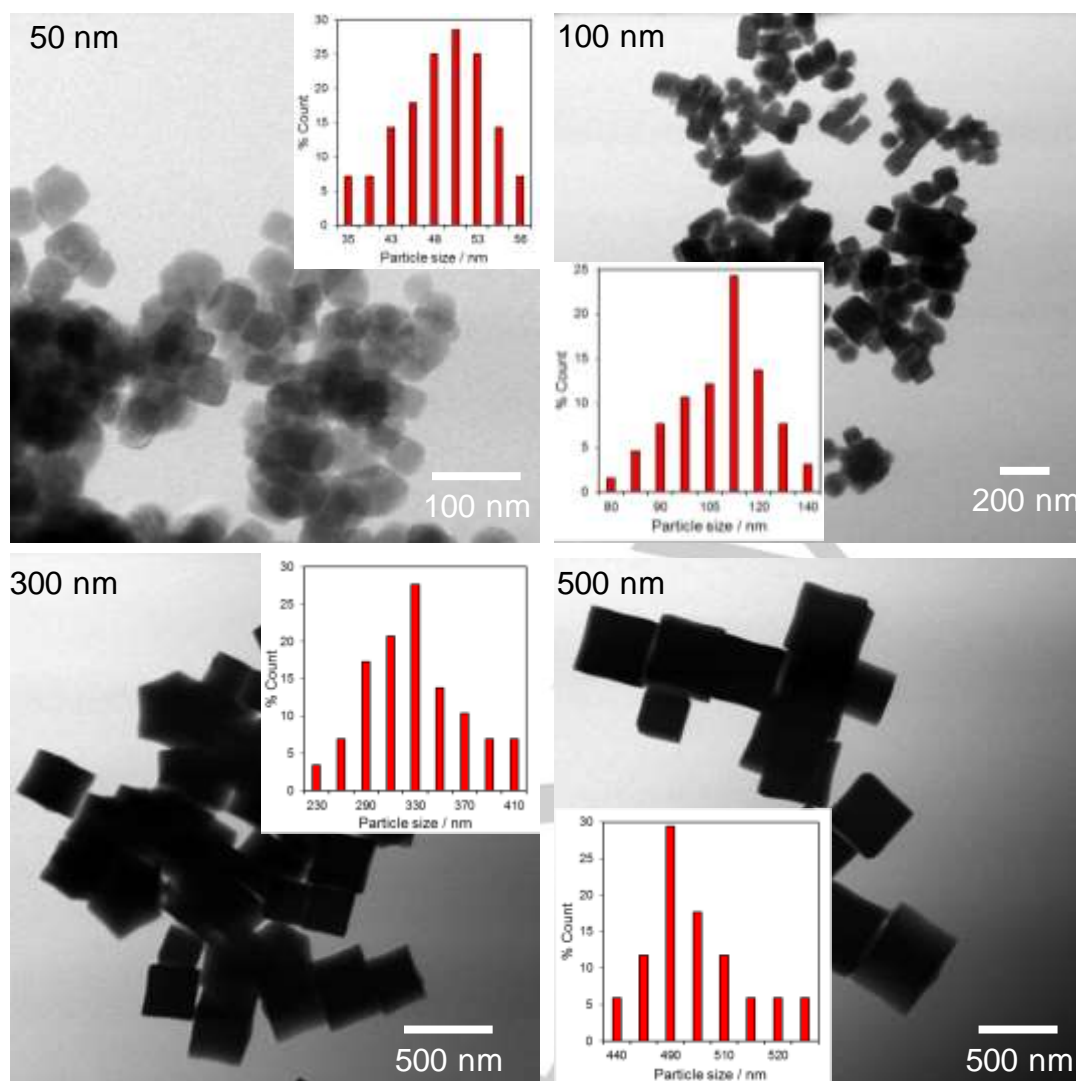
Figure 1. TEM images of Cu$_2$O nanocubes and (inset) corresponding particle size distributions.

quantum efficiency of 1.2 %, over 375 nm hierarchical Cu$_2$O nanocubes in the absence of any sacrificial donor.[28]

Herein we report a systematic investigation of the impact of Cu$_2$O size on both the photocatalytic degradation of aqueous organics, and production of H$_2$. Previous efforts to prepare monodispersed Cu$_2$O nanocubes of tunable size have utilised nitrate, sulphate or chloride precursors, and capping agents such as SDS, CTAB or PEG.[7, 14b, 14c, 29] However, access to a wide size range of Cu$_2$O nanostructures has to date required a seed-mediated approach, and there are no systematic studies of their corresponding size-structure-activity relationships.

A new synthetic route to monodispersed Cu$_2$O nanocubes with sizes spanning 50-500 nm employing an acetate precursor is described, enabling facile tuning of their photophysical properties and corresponding photocatalytic performance. Physicochemical properties were characterised by bulk and surface analytical methods including XRD, XPS, HRTEM, SEM, DRUVS, time-

resolved photoluminescence, and N$_2$ porosimetry. Optical band gaps, electronic band energies, rates of charge recombination, apparent quantum efficiency, and the surface copper oxidation state, all evolve monotonically with nanocube size, and correlate with photocatalytic activity towards aqueous phase phenol degradation, and hydrogen production, under visible light irradiation.

Results and Discussion

Photophysical characterisation
Successful synthesis of uniform Cu$_2$O nanocubes with tunable dimensions was first demonstrated using a simple solution phase approach with ascorbic acid as a reductant and PEG as a structure-directing agent. The morphology and size distribution of

FULL PAPER
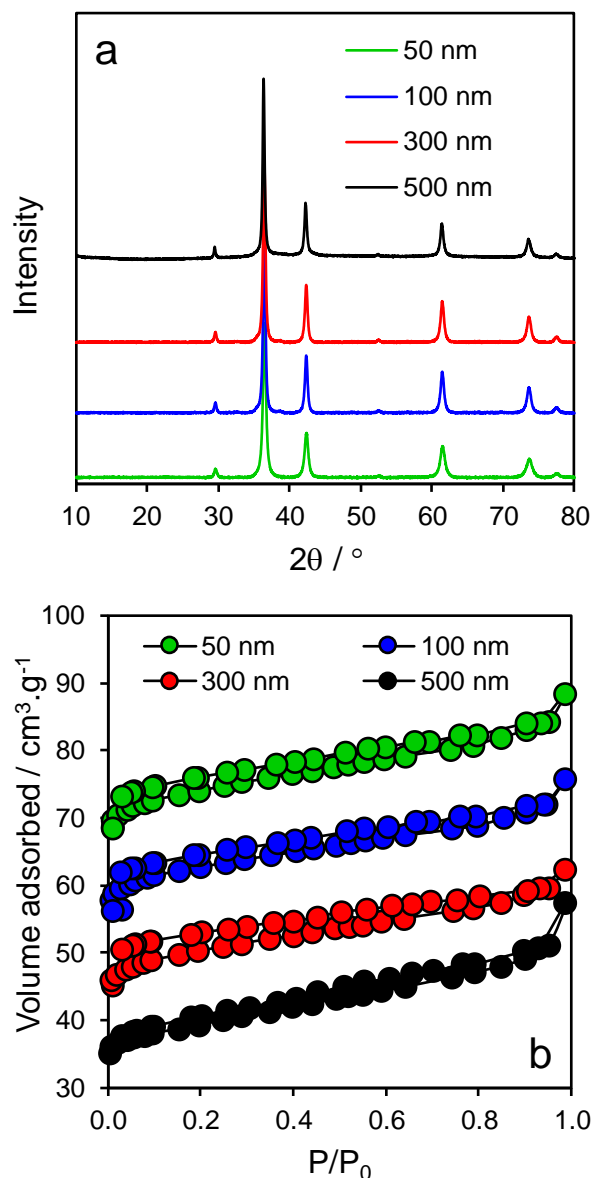
Figure 2. (a) XRD patterns, and (b) N₂ adsorption-desorption isotherm of Cu₂O nanocubes.

Cu₂O nanocubes was determined by TEM (Figure 1) and SEM (Figure S1) and revealed dense nanocubes with smooth surfaces and dimensions of between 50-500 nm. Cubes could be prepared with excellent monodispersity simply by increasing the PEG concentration, consistent with previous reports,[7] which shows that ligand capping concentration has an important role in controlling particle size and structure[30]. High resolution TEM images of the 300 nm Cu₂O nanocubes (Figure S2) reveal interplanar lattice spacings of 0.24 nm, indicative of (111) facets of cubic Cu₂O.[31]

The phase purity and crystallinity of the Cu₂O nanocubes was subsequently investigated by powder XRD (Figure 2a). All nanocubes exhibited peaks at 2θ= 29.6 °, 36.42 °, 42.31 °, 52.46 °,

61.38 °, 73.52 °, and 77.38 ° indexed as the (111), (200), (211), (220), (311), and (222) reflections of cubic Cu₂O (JCPDS #73-0687); no reflections attributable with either CuO or fcc Cu metal were observed. Volume-averaged crystallite sizes estimated from the Scherrer equation (Table 1) suggest that in all cases the dense Cu₂O nanocubes comprise compact agglomerations of 20-30 nm crystallites, whose size increased slightly with the overall nanocube dimensions. Textural properties were also examined by nitrogen porosimetry, with the resulting type II adsorption-desorption isotherms (Figure 2b) characteristic of macroporous materials (or non-porous materials possessing large interparticle voids) with very small H3-type hysteresis loops; corresponding BJH pore size distributions (Figure S3) confirmed that the nanocubes are essentially non-porous. BET surface areas decreased with increasing nanocube size, albeit not by the order of magnitude predicted by simple geometric considerations. Although small nanoparticles may be advantageous in photocatalysis due to their higher specific surface area,[32] other size-dependent factors such as the surface termination,[33] and mobility and recombination of photoexcited charge carriers may favour large particles.[34]

Optical properties of the Cu₂O nanocubes were determined by DRUVS (Figure 3a). All nanocubes exhibited strong absorbances between 200-500 nm, in close agreement with previous reports on Cu₂O nanocubes.[7, 14c] Corresponding Tauc plots (Figure 3b) were obtained using Equation 1:

$$\alpha h v = A(h v - E_g)^{\eta} \qquad (1)$$

where α, h, v, Eg, and A are the absorption coefficient, Planck's constant, light frequency, band gap energy, and a proportionality constant, respectively. As a direct band gap material $\eta = 0.5$ for Cu₂O, this enables the band gap to be calculated using absorption coefficients determined from the Kubelka-Munk formalism (Equation 2):

$$a = \frac{(1-R)^2}{2R} \qquad (4)$$

The resulting band gaps decreased with nanocube size from 2.25 eV to 1.96 eV (Table 1) consistent with literature values for Cu₂O nanostructures.[5a, 35] The electronic band structure of the Cu₂O nanocubes was determined by valence band XP measurements. Valence band maximum (VBM) energies, derived from the intercept of the tangent to the density of states at the Fermi edge (Figure S4a), decreased with increasing particle size from 0.81 (50 nm) to 0.35 eV (500 nm). This is in good agreement with XPS and optical absorption studies of Cu₂O nanoparticles prepared by reactive evaporation, attributed to an increase in the dopant ionization energy and associated shift in the Fermi level.[36] Corresponding conduction band minimum (CBM) energies, derived from these VBM and the optical band gap energies spanned -1.44 eV to -1.61 eV, significantly greater than that required for hydrogen reduction (-0.65 eV at pH 7).[37]

The oxidation state of copper in the nanocubes was explored by Cu 2p XP spectra (Figure S4b), which evidence a strong size-dependence. Small cubes exhibit sharp photoemission features at 932.3 and 951.8 eV binding energy, consistent with the spin-orbit split 2p₃/₂ and 2p₁/₂ components of Cu₂O and/or copper metal;[5a] the latter can be discounted since there is no evidence of metallic copper from XRD. In addition, the 50-300 nm nanocubes exhibit a second weak 2p spin-orbit split
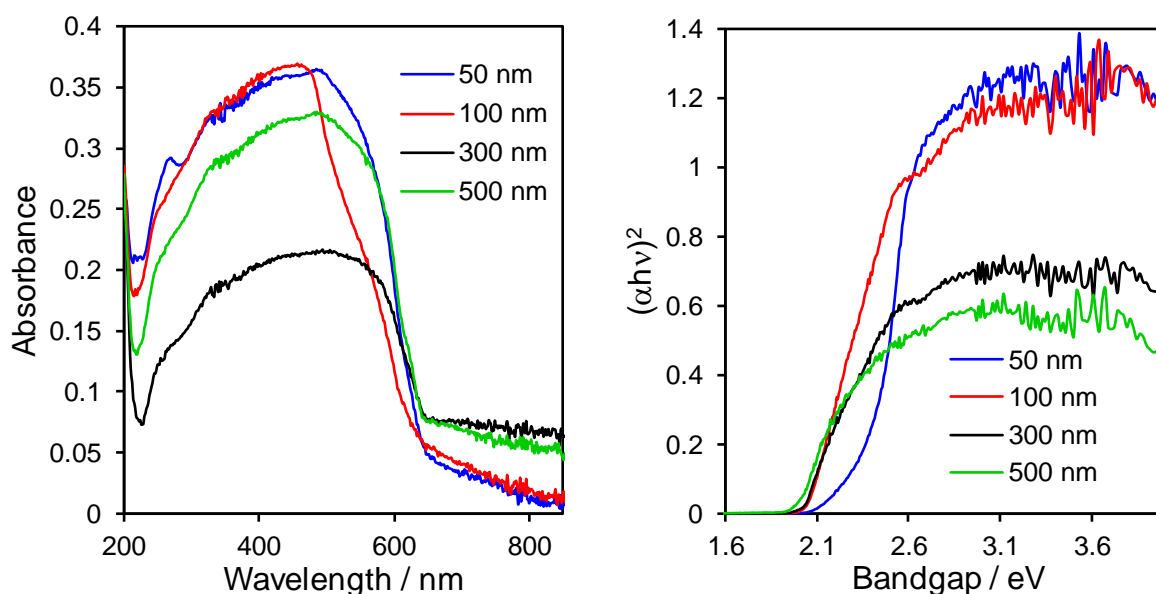
FULL PAPER

Table 1. Physicochemical properties of Cu_2O nanocubes.

Nanocube size / nm[a]	Crystallite size[b] / nm	BET surface area / $m^2.g^{-1}$[c]	Band gap / eV[d]	CBM[e] / eV	Cu(I)[f] / atom%	Cu(I):Cu(II)[f]
50	18.5	20	2.25	-1.44	77.1	3.4
100	25.3	19	2.10	-1.56	80.8	4.2
300	26.7	15	2.05	-1.60	81.3	4.5
500	29.3	13	1.96	-1.61	89.6	8.6

[a] TEM. [b] XRD. [c] N_2 porosimetry. [d] DRUVS. [e] calculatyed from valence band XPS and DRUVS. [f] Cu 2p XPS.


Figure. 3. (a) DRUVS absorption spectra, and (b) corresponding Tauc plot of Cu_2O nanocubes.

doublet at 935.6 eV and 955.4 eV, accompanied by a weak 943 eV satellite feature, both characteristic of $Cu(OH)_2$ (these features are almost absent for the 500 nm cubes).[38] Spectral fitting reveals that the proportion of Cu_2O relative to $Cu(OH)_2$ increased monotonically from 77.1 % in the 50 nm sample to 89.6 % for the 500 nm nanocubes. Recombination of photoexcited charge carriers within the Cu_2O nanocubes was subsequently investigated by steady state (Figure 4a) and time-resolved (Figure 4b) photoluminescence (PL). For 560 nm excitation, the principal emission at 620 nm (Figure 4a) was inversely proportional to particle size, indicative of slower radiative recombination of photoexcited electron-hole pairs for the larger cubes.[39] This conclusion is supported by corresponding time-resolved PL decay spectra (Figure 4b) which exhibited longer radiative lifetimes for the 500 nm (τ_1=0.628 ns) versus 50 nm (τ_1=0.585 ns) nanocubes (Table 2).[4, 40]

Table 2. Fitted parameters from time-resolved photoluminescence for Cu_2O nanocubes.

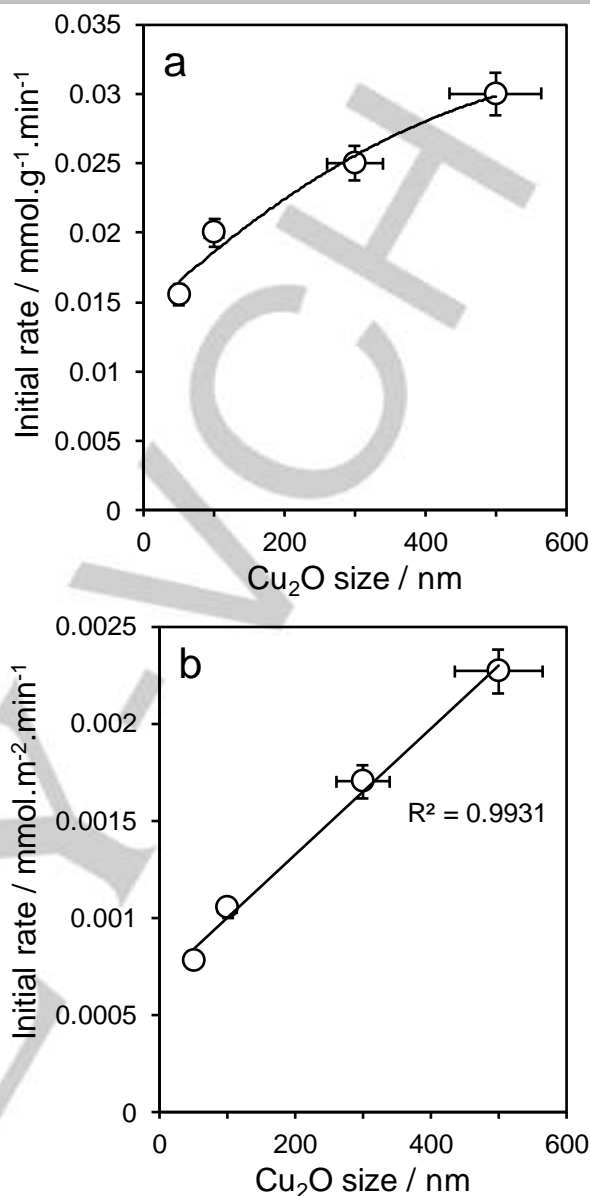| Nanocube size / nm[a]	τ_1 / ns	B_1[b]	χ^2[c]
50	0.585	361.2	1.44
100	0.619	364.1	1.38
300	0.628	192	1.19
500	0.628	143.1	1.18

FULL PAPER
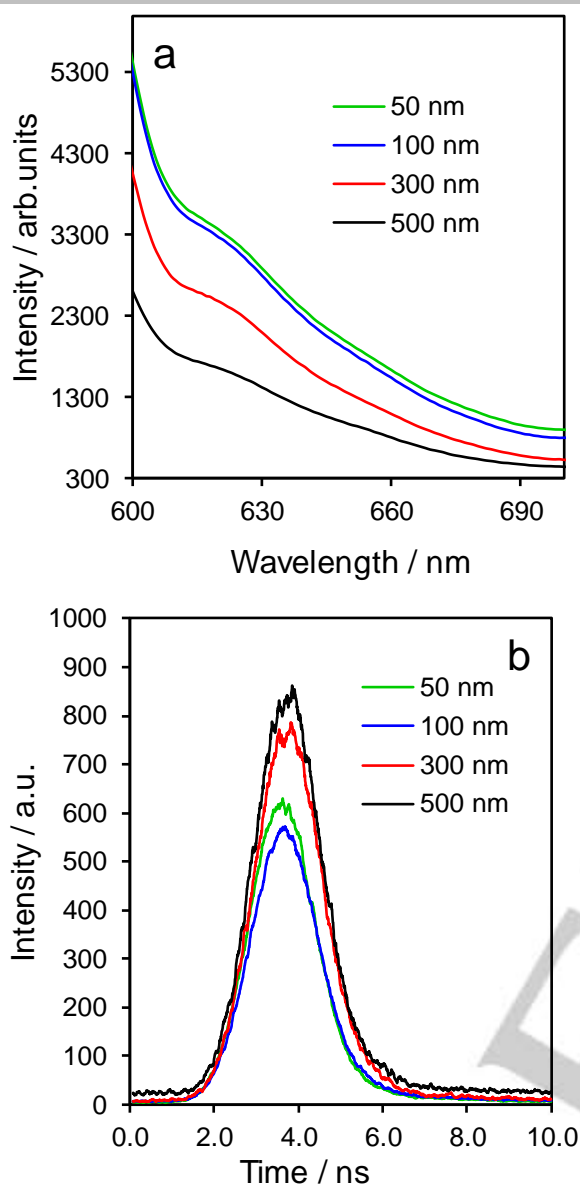
Figure 4. (a) Steady state, and (b) time-resolved PL spectra of Cu₂O nanocubes under 560 nm excitation.

Figure 5. (a) Mass normalised, and (b) surface area normalised initial rates of phenol degradation over Cu₂O nanocubes under visible light. Experimental conditions: 0.127 mmol phenol in 50 mL water, 20 mg catalyst, 200 W Hg-Xe arc lamp with 420 nm visible cut-off filter, 15 min reaction.

Photocatalytic phenol degradation

The photocatalytic performance of the family of Cu₂O nanocubes was first studied for the aqueous phase degradation of phenol under visible light irradiation. In addition to being a prototypical organic pollutant,[41] phenol has negligible absorbance in the visible region, and hence is not prone to the artefacts that arise in dye degradation studies due to catalyst sensitisation (which in turn hinder mechanistic insight and performance benchmarking).[42] The resulting reaction profiles (Figure S5) reveal only a small (<10 %) contribution from photolysis in the absence of photocatalyst. Corresponding initial rates of phenol degradation reveal a direct relationship between nanocube size and both specific (mass-) and surface area normalised degradation rates (Figure 5); increasing cube size from 50 to

500 nm results in a three-fold enhancement in photocatalytic activity. The linear relationship between the surface area normalised degradation rate (essentially the turnover frequency) and nanocube size demonstrates that phenol decomposition is heavily influenced by either bulk electronic properties (e.g. band gap, CBM, and/or rate of charge carrier recombination) or the surface density of Cu(I) species, rather than a unique structure-sensitivity to (100) facets. Similar observations are reported for WO₃ nanoparticles towards photocatalytic water oxidation, wherein a four-fold rate-enhancement in the specific activity was observed upon increasing particle size from 100 to 800 nm

FULL PAPER
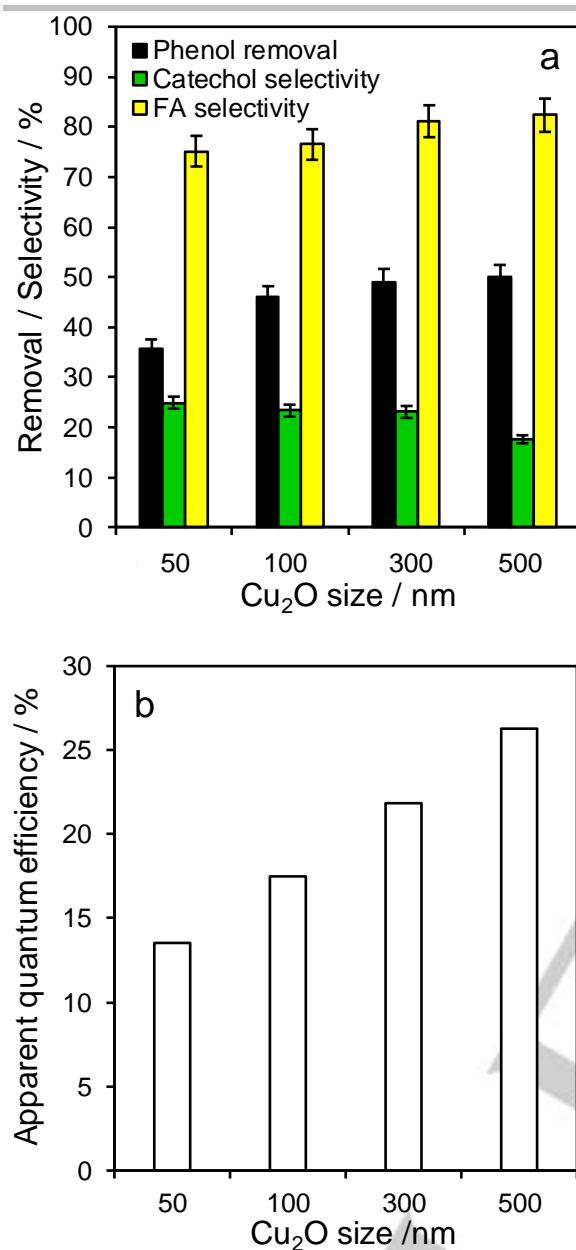
Figure 6. (a) Phenol removal and relative selectivity to organic by-products over Cu$_2$O nanocubes under visible light, and (b) corresponding apparent quantum efficiency. Experimental conditions: 0.127 mmol phenol in 50 mL water, 20 mg catalyst, 200 W Hg-Xe arc lamp with 420 nm visible cut-off filter, 240 min reaction.

particles, attributed to slower surface recombination of photogenerated electrons and holes.[34] Smaller semiconductor nanoparticles often exhibit high defect densities (notably surface defects), which may promote undesired e$^-$-h$^+$ charge carrier surface recombination, or the creation of new states localised within the band gap that trap photogenerated charge carriers, thereby lowering photocatalytic activity.[33] The first order rate constant for phenol degradation over the 500 nm Cu$_2$O cubes of 0.009 min^{-1} significantly exceeds literature reports for alternative metal oxide photocatalysts (Table S1),[43] which also typically

employ higher power light sources and catalyst loadings than the present work.

A critical and oft-neglected aspect of photocatalytic depollution studies is the fate of organic reactants, i.e. the nature of the resulting degradation products, with most literature reports simply assuming complete mineralisation.[43] The phenol degradation pathway, and possible role of in-situ generated radicals, was therefore subsequently investigated by HPLC as a function of Cu$_2$O nanocube size, with catechol and fumaric acid identified as the principal organic by-products after 240 min irradiation. As anticipated, for all nanocube sizes catechol appears as the primary product of phenol oxidation, being itself consumed at longer reaction times, whereas fumaric acid is formed throughout the reaction as a secondary decomposition product (Figure 6a). Tryba et al report that the formation of catechol as a primary product of phenol decomposition (rather than hydroquinone or benzoquinone) favours subsequent carboxylic acid formation and mineralisation.[44] The greater rate observed for increasing nanocube size from 50 to 500 nm leads to enhanced phenol removal from 36 to 50 % after 6 h, and concomitant absolute selectivity to fumaric acid from 7.8 to 25 %. The latter observation is significant since the toxicity of fumaric acid is far lower than that of catechol, with LD50 Oral of ~10,500 mg.kg^{-1} and 250 mg.kg^{-1} respectively.[45] Apparent quantum efficiencies (see Supporting Information for calculation) tracked the rates of phenol degradation, increasing from 14 to 26 % with Cu$_2$O nanocube size (Figure 6b). The latter value is 1500 times that reported for Pt/TiO$_2$ under UV irradiation.[46]

The photocatalytic oxidation of phenol to catechol and fumaric acid likely occurs through hydroxyl radicals which initially form hydroxyl substituted aromatic derivatives,[47] with negligible hydroquinone detected (which exists in equilibrium with benzoquinone). Hydroxyl radical attack is proposed to follow previous reports[48] as summarised in Scheme 1, and initiated by hydroxyl radical formation at the photocatalyst surface via reaction of photoexcited holes with hydroxide ions.[49] Concomitant superoxide radical anion (O$_2^{\bullet-}$) formation can occur through the reduction of O$_2$ via photoexcited electrons from the conduction band,[50] which in turn reacts with water to form H$_2$O$_2$, another strong oxidant.

Catalyst stability towards visible light driven phenol degradation was assessed for the 300 nm Cu$_2$O nanocubes over multiple recycles. Figure 7a evidenced negligible activity loss over four consecutive reactions, consistent with retention of the initial crystallinity and particle size observed by XRD (Figure 7b), and hence excellent long-term stability. Photocorrosion is often problematic for Cu$_2$O photocatalysts, and hence the size and morphology of 300 nm nanocubes was examined by SEM and TEM post-reaction following aqueous phase phenol degradation. The resulting micrographs (Figure S6) evidence no significant changes in either particle size or shape following photocatalytic phenol degradation, confirming the stability of our Cu$_2$O nanocubes, consistent with Figure 7a. Corresponding Cu 2p XP spectra also show little increase in the 943 eV Cu(II) satellite (Figure S7) post-reaction.

FULL PAPER
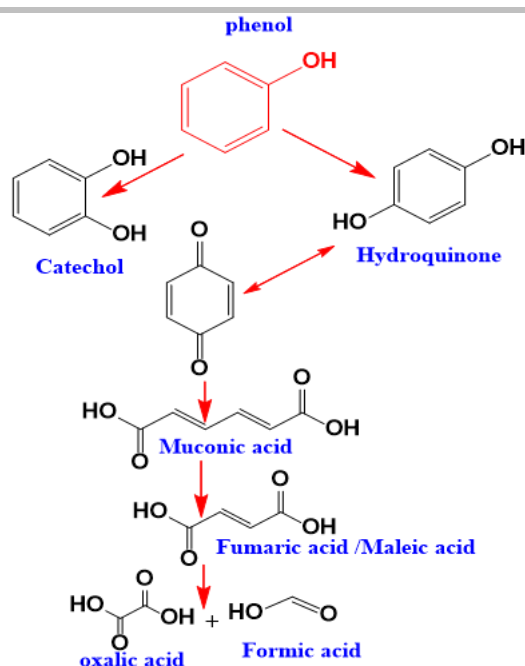
Scheme 1. Proposed pathways for photocatalytic phenol degradation over Cu$_2$O nanocubes under visible light.

Photocatalytic hydrogen production

Cuprous oxide has been proposed as a promising candidate for photo-assisted water splitting, due to its favourable conduction band position for proton reduction, although its shallow valence band only offers (at best) a low overpotential for water oxidation.[37, 51] Since the measured CBM energies for our Cu$_2$O nanocubes far exceed that required for proton reduction (>1.5 eV versus -0.4 eV), their performance was therefore assessed for photocatalytic H$_2$ production in the presence of a 1 wt% platinum co-catalyst and Na$_2$SO$_3$ as a hole scavenger. HRTEM of the platinised 300 nm Cu$_2$O nanocube revealed highly dispersed and uniform 0.6-1.2 nm Pt nanoparticles (Figure S8 a-b). The resulting visible light photocatalytic activity (Figure 8a-b) reveals a similar size-dependency as observed for phenol degradation; specific (mass-normalised) and surface area normalised H$_2$ productivity are proportional to particle size. These trends mirror the corresponding rise in CBM energy (Table 1), a key parameter in controlling activity,[52] and apparent quantum efficiency (Figure S9, which reached 1.2 % for 500 nm Cu$_2$O), across the nanocube family. This performance is comparable to that of Hara and co-workers who observed 0.16 μmolg^{-1}h^{-1} over unstructured 300-500 nm Cu$_2$O particles, but with an apparent quantum efficiency of only 0.3 %.[53]

Charge recombination is believed to play an important role in regulating photocatalytic reactivity. Hence the question arises whether the variation in charge carrier lifetimes between different nanocubes accounts for their size-dependent photocatalytic activity. If so, then normalising hydrogen productivity to the charge recombination rates from time-resolved photoluminescence spectroscopy (Table 2) should result in a common value for all photocatalysts. Such normalisation does not yield a common value (Figure S10), and hence charge carrier lifetimes do not dominate our photocatalyst performance.
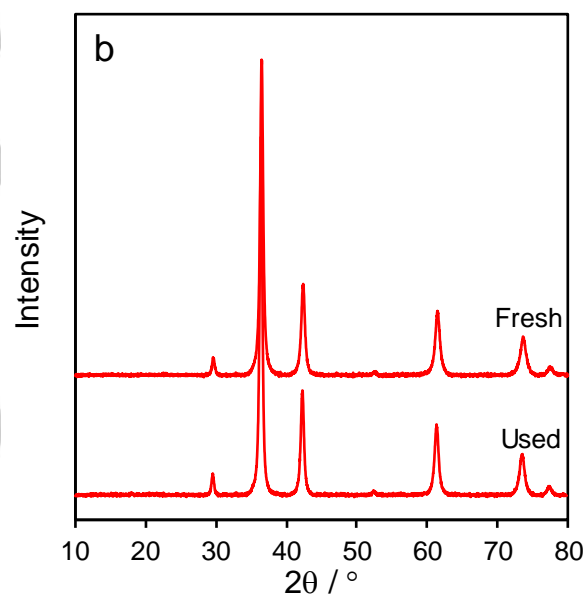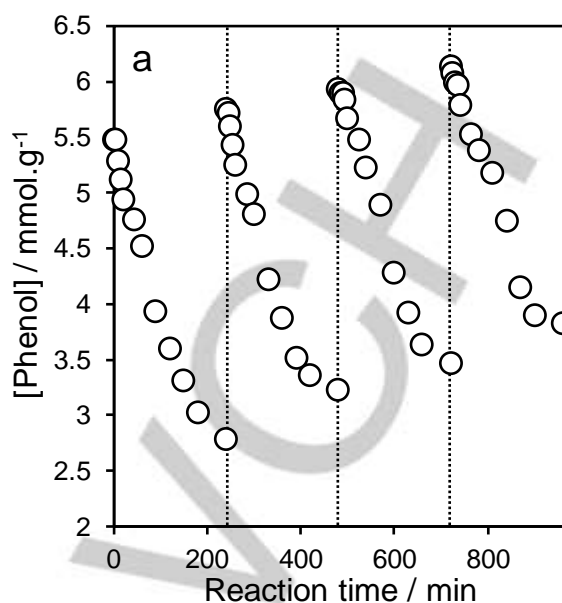

Figure 7. (a) Photocatalyst stability during phenol degradation over 300 nm Cu$_2$O nanocubes under visible light, and (b) corresponding powder XRD of fresh and used nanocubes following four consecutive reactions. Experimental conditions: 0.127 mmol phenol in 50 mL water, 20 mg catalyst, 200 W Hg-Xe arc lamp with 420 nm visible cut-off filter.

Conclusions

A new one-pot, solution phase synthesis offers uniform Cu$_2$O nanocubes of tunable size between 50 to 500 nm. Nanocube photophysical properties, notably the optical band gap, conduction band minimum, and charge-carrier recombination rate, evolve continuously with particle size and are closely correlated with visible light photocatalytic activity for phenol degradation and H$_2$ production. Despite their lower surface area,

FULL PAPER
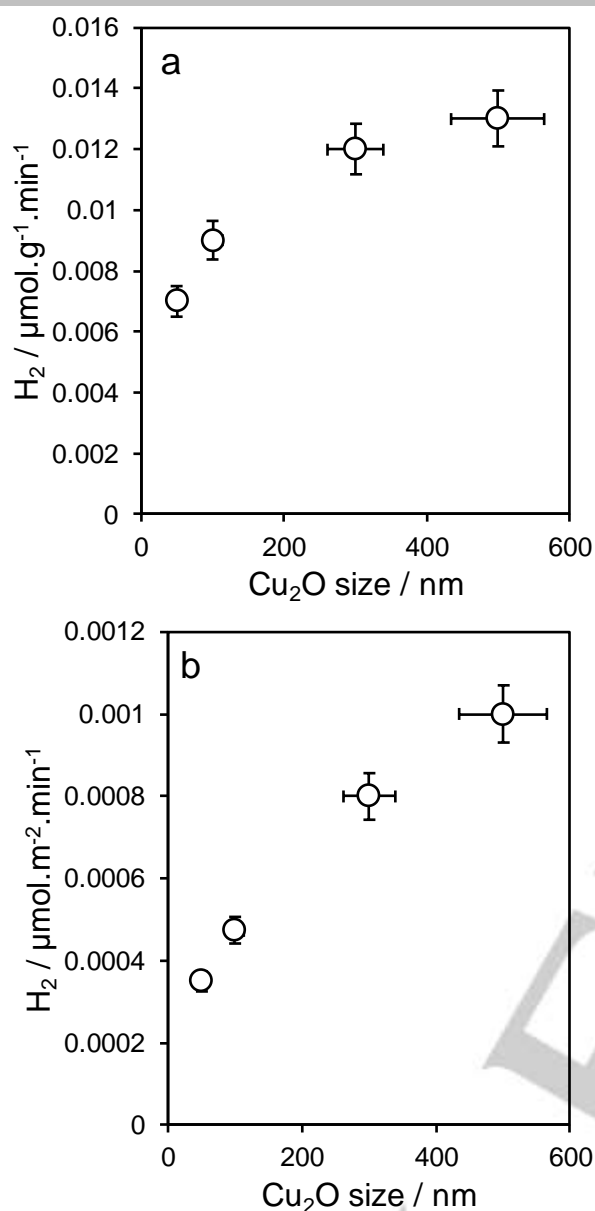
Figure 8. a) Photocatalytic hydrogen evolution under visible light, b) surface area normalised rates of hydrogen production over 1 wt% Pt promoted Cu_2O nanocubes (experimental conditions: 50 mL water, 50 mg catalyst, 200 W Hg-Xe arc lamp with 420 nm visible cut-off filter, 5 h reaction.

larger Cu_2O nanocubes offer superior phenol mineralisation, and selectivity to more benign by-products (fumaric acid versus catechol), and also exhibit excellent stability over four consecutive re-uses. Future work will explore the impact of Cu_2O shape and facet on photoactivity.

Experimental Section

Chemicals

Copper (II) acetate (Aldrich, 98.0 %), NaOH (Aldrich, ≥98 %), L-ascorbic acid (Aldrich, 99 %), polyethylene glycol (Alfa Aesar, MW 600), hexachloroplatinic (IV) acid hydrate (Aldrich, 99.9 %), phenol (Aldrich, 99 %) acetonitrile HPLC grade (Sigma, 99.93 %) and sodium sulfate (Sigma, 99 %) were used without further purification. Deionised water was used for all solution preparation.

Cu_2O nanocube synthesis

A range of Cu_2O nanocubes were prepared by a solution phase approach. Typically, 5 mL of 0.02 M copper acetate was mixed with 6 mL of 0.04 M polyethylene glycol during continuous stirring at 550 rpm and 65 °C for 10 min, resulting in a deep blue solution. In a separate vessel, 2 mL of 1 M NaOH and 2 mL of 0.05 M ascorbic acid were mixed with 35 mL of deionised water. The NaOH/ascorbic acid mixture was then added dropwise to the copper acetate/PEG solution, and stirring continued at 65 °C for another 5 min. The mixture was then transferred to a sealed round bottom flask and purged with N_2 for 30 min to allow formation of a brownish-yellow Cu_2O nanocube precipitate. The nanocubes were isolated by 7 min centrifugation at 8000 rpm, washed twice with H_2O, and three times with ethanol to remove any residual PEG, and finally dried overnight at 65 °C and stored in air. Different size nanocubes were prepared with side lengths between 50 and 500 nm by changing the volume of PEG between 2-9 mL respectively. The synthesis is summarised in Scheme 2: PEG first complexes to the Cu(II) ions which are subsequently reduced on ascorbic acid addition, and precipitated as Cu(I) oxide in the presence of NaOH; hydroxyl groups in the PEG matrix are likely responsible for controlling the density of Cu ions and resulting Cu_2O nanocube dimensions.[5a, 7]
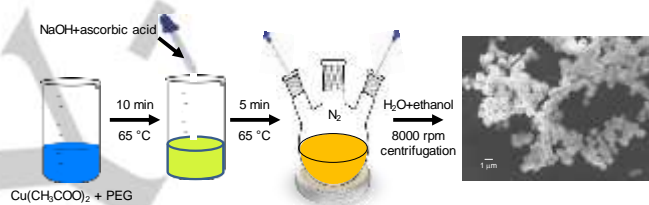
Scheme 2. Synthesis of Cu_2O nanocubes.

Pt functionalisation of Cu_2O nanocubes

Cu_2O nanocubes were also functionalised with a Pt co-catalyst by in-situ photodeposition to aid water splitting.[54] 100 mg Cu_2O nanocubes were dispersed in 20 mL deionised water, to which 30 mL methanol and an appropriate amount of aqueous H_2PtCl_6 was added (2.10 mg of H_2PtCl_6 in 20 mL deionised water, equating to a nominal 1 wt% Pt loading). The resulting mixture was ultrasonicated for 5 min, and then irradiated by a 200 W Hg-Xe light source for 1 h under stirring within a stainless steel reactor. The Pt/Cu_2O nanocubes were then separated by centrifugation and dried in vacuo at 65 °C for 6 h.

Catalyst characterisation

Crystallinity was examined by powder X-ray diffraction (XRD) using a Bruker-AXS D8 ADVANCE diffractometer operated at 40 kV and 40 mA and Cu K_α radiation (λ=0.15418 nm) between 2θ= 10-80° in 0.02° steps. X-ray photoelectron spectroscopy (XPS) was performed on a Kratos Axis HSi spectrometer with monochromated Al K_α X-ray source operated at 90 W and normal emission, employing magnetic focusing and a charge neutraliser. Spectra were fitted using CasaXPS version 2.3.16, with energy referencing to adventitious carbon at 284.6 eV, and surface compositions derived through applying appropriate instrumental response factors. Cu_2O and Pt/Cu_2O nanocubes were visualised using a JEOL JEM-2100 TEM microscope operated at 200 kV. Brunauer–Emmett–Teller (BET) surface areas were obtained by N_2 physisorption at 77 K using a Quantachrome NOVA 4000e porosimeter on samples degassed at 120 °C for 4 h. Surface areas were calculated over the relative pressure range 0.01-0.2, and BJH pore size distributions calculated from the desorption branch of the isotherm for relative pressures >0.35. Diffuse reflectance UV–vis absorption spectra (DRUVS) were recorded on a Thermo Scientific Evo220 spectrometer using an integrating sphere, and KBr as a standard,

FULL PAPER

with band gaps determined between 200-800 nm. Steady state photoluminescence (PL) spectra of Cu_2O were measured on a F-4500FL spectrophotometer using 560 nm excitation. Time-resolved photoluminescence (TRPL) spectra were measured on an Edinburgh Photonics FLS 980 spectrometer using pulsed picosecond LED light and 560 nm excitation. Phenol concentrations were determined by HPLC using an Agilent 1260 Infinity Quaternary HPLC equipped with both a UV diode array and refractive index detectors; an Agilent Zorbax Eclipse plus C18 column was employed at 35 °C, with 25 μL injection volume, and 1 mL/min of a 10 vol% acetonitrile/90 vol% water (HPLC grade) mobile phase, and 270 nm detection wavelength.

Photocatalytic oxidation of phenol

Photocatalytic phenol oxidative degradation was performed under visible light in a sealed 260 mL quartz photoreactor at room temperature. 20 mg of as-prepared Cu_2O nanocubes were dispersed by 5 min ultrasonication in 50 mL of 0.127 mM aqueous phenol solution in the dark, and then stirred for a further 60 min to equilibrate any phenol adsorption prior to irradiation. The mixture was then irradiated by a 200 W Hg-Xe arc lamp (Oriel Instruments 66002) using a 420 nm filter to remove UV light. The flux inside the reactor was 16.7 mW.cm^{-2}. 1 mL aliquots of the reaction mixture were periodically withdrawn for HPLC analysis. The spent catalyst was separated from the reaction mixture by 7 min centrifugation at 8000 rpm, dried, and stored in air prior to characterisation. The concentration of phenol, and catechol and fumaric acid by-products were analysed by HPLC (with response factors determined from multi-point calibration curves). Phenol photodegradation and organic product selectivities were calculated from Equations 3 and 4. Reactions were performed in triplicate, with resulting mean values and standard deviations presented.

$$\text{Phenol removal efficiency (conversion)} = \qquad (3)$$
$$100 \times ([\text{Phenol}]_{initial} - [\text{Phenol}]_{final})$$

$$\text{Selectivity} / \% = 100 \times (\text{mmol}_{Product} / \text{mmol}_{Phenol\ converted}) \qquad (4)$$

Photocatalytic hydrogen production

Water splitting was performed using the same reactor and light source as for phenol degradation. 50 mg of Pt/Cu_2O nanocubes were dispersed by 5 min ultrasonication in a 50 mL aqueous solution of 0.5 M Na_2SO_3 (as a hole scavenger). The reaction mixture was degassed with He for 1 h and reactor purged of air. Aliquots of the reactor headspace were periodically withdrawn in a 1 mL gas-tight syringe for GC analysis using a Shimadzu Tracera GC-2010 Plus gas chromatograph fitted with a Carboxen1010 column (30 m× 0.53 mm × 0.1 μm) and barrier ionization detector employing He carrier gas.

For both reactions, mass-normalised photocatalytic activities are reported to enable quantitative benchmarking of different catalysts. As Machmeyer and Che have expounded,[55] intrinsic reaction kinetics of photocatalytic reactions can only be determined in regimes wherein the rate of reactant conversion is directly proportional to the catalyst mass; if this is not the case, then the activity observed may reflect limited access to e.g. reactants, water, sacrificial reagents (if applicable), or photons due to self-absorption/scattering. The latter may occur when optimising catalyst concentrations to maximise light absorption.[56] Apparent quantum efficiencies were determined using a 475 nm band-pass filter and associated light intensity within the reactor. Calculation details are provided in the Supporting Information.

Acknowledgements

Conflict of Interest

The authors declare no conflict of interest.

[1] M. R. Hoffmann, S. T. Martin, W. Choi, D. W. Bahnemann, *Chem. Rev.* **1995**, *95*, 69-96.

[2] P. D. Tran, L. H. Wong, J. Barber, J. S. Loo, *Energy Environ. Sci.* **2012**, *5*, 5902-5918.

[3] a) T. Inoue, A. Fujishima, S. Konishi, K. Honda, *Nature* **1979**, *277*, 637-638; b) D. Chen, X. Zhang, A. F. Lee, *J. Mater. Chem A* **2015**, *3*, 14487-14516.

[4] Y. Pan, S. Deng, L. Polavarapu, N. Gao, P. Yuan, C. H. Sow, Q.-H. Xu, *Langmuir* **2012**, *28*, 12304-12310.

[5] a) S. Kumar, C. M. Parlett, M. A. Isaacs, D. V. Jowett, R. E. Douthwaite, M. C. Cockett, A. F. Lee, *Appl. Catal. B* **2016**, *189*, 226-232; b) S. Sun, *Nanoscale* **2015**, *7*, 10850-10882.

[6] P. Basnet, Y. Zhao, *Catal. Sci. Technol.* **2016**, *6*, 2228-2238.

[7] L. Gou, C. J. Murphy, *J. Mater. Chem.* **2004**, *14*, 735-738.

[8] M. J. Siegfried, K.-S. Choi, *J. Am. Chem. Soc.* **2006**, *128*, 10356-10357.

[9] M. Leng, M. Liu, Y. Zhang, Z. Wang, C. Yu, X. Yang, H. Zhang, C. Wang, *J. Am. Chem. Soc.* **2010**, *132*, 17084-17087.

[10] C. Lu, L. Qi, J. Yang, X. Wang, D. Zhang, J. Xie, J. Ma, *Adv. Mater.* **2005**, *17*, 2562-2567.

[11] H. Xu, W. Wang, *Angew. Chem. Int. Ed.* **2007**, *46*, 1489-1492.

[12] a) W.-C. Huang, L.-M. Lyu, Y.-C. Yang, M. H. Huang, *J. Am. Chem. Soc.* **2011**, *134*, 1261-1267; b) Y. Shang, Y. M. Shao, D. F. Zhang, L. Guo, *Angew. Chem. Int. Ed.* **2014**, *53*, 11514-11518; c) J. Lin, Y. Shang, X. Li, J. Yu, X. Wang, L. Guo, *Adv. Mater.* **2017**, *29*.

[13] a) R. Li, X. Yan, L. Yu, Z. Zhang, Q. Tang, Y. Pan, *CrystEngComm* **2013**, *15*, 10049-10058; b) H. Xu, W. Wang, W. Zhu, *J. Phys. Chem. B* **2006**, *110*, 13829-13834.

[14] a) P. Lignier, R. Bellabarba, R. P. Tooze, *Chem. Soc. Rev.* **2012**, *41*, 1708-1720; b) L. Gou, C. J. Murphy, *Nano Lett.* **2003**, *3*, 231-234; c) C. H. Kuo, C. H. Chen, M. H. Huang, *Avd. Funct. Mater.* **2007**, *17*, 3773-3780.

[15] a) T. Deblonde, C. Cossu-Leguille, P. Hartemann, *Int. J. Hyg. Environ. Health* **2011**, *214*, 442-448; b) Y. J. Chan, M. F. Chong, C. L. Law, D. G. Hassell, *Chem. Eng. J.* **2009**, *155*, 1-18.

[16] a) S. D. Richardson, T. A. Ternes, *Anal. Chemistry* **2014**, *86*, 2813-2848; b) N. Bolong, A. F. Ismail, M. R. Salim, T. Matsuura, *Desalination* **2009**, *239*, 229-246; c) M. Stuart, D. Lapworth, E. Crane, A. Hart, *Sci. Total Environ.* **2012**, *416*, 1-21.

[17] L. Yang, S. Luo, Y. Li, Y. Xiao, Q. Kang, Q. Cai, *Environ. Sci. Technol.* **2010**, *44*, 7641-7646.

[18] a) S. Esplugas, J. Gimenez, S. Contreras, E. Pascual, M. Rodríguez, *Water Res.* **2002**, *36*, 1034-1042; b) M. Pera-Titus, V. García-Molina, M. A. Baños, J. Giménez, S. Esplugas, *Appl. Catal. B* **2004**, *47*, 219-256; c) T. Olmez-Hanci, I. Arslan-Alaton, *Chem. Eng. J.* **2013**, *224*, 10-16; d) Z. Wang, W. Cai, X. Hong, X. Zhao, F. Xu, C. Cai, *Appl. Catal. B* **2005**, *57*, 223-231.

[19] S. Esplugas, J. Giménez, S. Contreras, E. Pascual, M. Rodríguez, *Water Res.* **2002**, *36*, 1034-1042.

[20] a) J. Schneider, M. Matsuoka, M. Takeuchi, J. Zhang, Y. Horiuchi, M. Anpo, D. W. Bahnemann, *Chem. Rev.* **2014**, *114*, 9919-9986; b) H. G. Oliveira, D. C. Nery, C. Longo, *Appl. Catal. B* **2010**, *93*, 205-211.

[21] E. Carpio, P. Zúñiga, S. Ponce, J. Solis, J. Rodriguez, W. Estrada, *J. Mol. Catal. A* **2005**, *228*, 293-298.
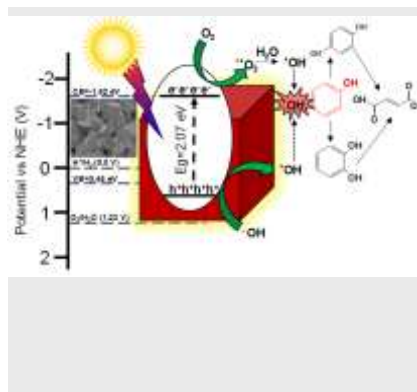
FULL PAPER

[22] a) Z.-h. Yuan, J.-h. Jia, L.-d. Zhang, *Mater. Chem. Phys.* **2002**, *73*, 323-326; b) W. Zhang, Y. Zhou, C. Dong, B. Shen, M. Xing, J. Zhang, *Res. Chem. Intermediat.* **2018**; c) S. Liu, X. Chen, *J. Hazardous Mater.* **2008**, *152*, 48-55.

[23] V. Vaiano, M. Matarangolo, J. J. Murcia, H. Rojas, J. A. Navío, M. C. Hidalgo, *Appl. Catal. B* **2018**, *225*, 197-206.

[24] H. Wang, Y. Liang, L. Liu, J. Hu, W. Cui, *J. Hazard. Mater.* **2018**, *344*, 369-380.

[25] M. Hara, T. Kondo, M. Komoda, S. Ikeda, J. N. Kondo, K. Domen, M. Hara, K. Shinohara, A. Tanaka, *Chem. Commun.* **1998**, 357-358.

[26] Y.-F. Zhao, Z.-Y. Yang, Y.-X. Zhang, L. Jing, X. Guo, Z. Ke, P. Hu, G. Wang, Y.-M. Yan, K.-N. Sun, *J. Phys. Chem. C* **2014**, *118*, 14238-14245.

[27] J. Chen, S. Shen, P. Guo, M. Wang, P. Wu, X. Wang, L. Guo, *Appl. Catal. B* **2014**, *152-153*, 335-341.

[28] S. Kumar, C. M. A. Parlett, M. A. Isaacs, D. V. Jowett, R. E. Douthwaite, M. C. R. Cockett, A. F. Lee, *Appl. Catal. B* **2016**, *189*, 226-232.

[29] L. Chen, Y. Zhang, P. Zhu, F. Zhou, W. Zeng, D. D. Lu, R. Sun, C. Wong, *Sci. Rep.* **2015**, *5*, 9672.

[30] Y. Xu, X. Jiao, D. Chen, *J. Phys. Chem. C* **2008**, *112*, 16769-16773.

[31] L. Liao, B. Yan, Y. Hao, G. Xing, J. Liu, B. Zhao, Z. Shen, T. Wu, L. Wang, J. Thong, *Appl. Phys. Lett.* **2009**, *94*, 113106.

[32] N. Xu, Z. Shi, Y. Fan, J. Dong, J. Shi, M. Z.-C. Hu, *Ind. Eng. Chem. Res.* **1999**, *38*, 373-379.

[33] X. Bai, J. Wei, B. Tian, Y. Liu, T. Reiss, N. Guiblin, P. Gemeiner, B. Dkhil, I. C. Infante, *J. Phys. Chem. C* **2016**, *120*, 3595-3601.

[34] F. Amano, E. Ishinaga, A. Yamakata, *J. Phys. Chem. C* **2013**, *117*, 22584-22590.

[35] K. E. Brown, K.-S. Choi, *Chem. Commun.* **2006**, 3311-3313.

[36] a) B. Balamurugan, I. Aruna, B. Mehta, S. Shivaprasad, *Phys. Rev. B* **2004**, *69*, 165419; b) J. Liu, J. Ke, D. Li, H. Sun, P. Liang, X. Duan, W. Tian, M. O. Tade, S. Liu, S. Wang, *ACS Appl. Mater. Interfaces* **2017**, *9*, 11678-11688; c) M. Yang, L. Zhu, Y. Li, L. Cao, Y. Guo, *J. Alloy Compd.* **2013**, *578*, 143-147; d) Y. Jiang, H. Yuan, H. Chen, *PCCP* **2015**, *17*, 630-637.

[37] P. E. de Jongh, D. Vanmaekelbergh, J. J. Kelly, *Chem. Commun.* **1999**, 1069-1070.

[38] a) J. Ghijsen, L. H. Tjeng, J. van Elp, H. Eskes, J. Westerink, G. A. Sawatzky, M. T. Czyzyk, *Phys. Rev. B* **1988**, *38*, 11322-11330; b) J. P. Espinós, J. Morales, A. Barranco, A. Caballero, J. P. Holgado, A. R. González-Elipe, *J. Phys. Chem. B* **2002**, *106*, 6921-6929.

[39] a) I. Mukherjee, S. Chatterjee, N. A. Kulkarni, *J. Phys. Chem. C* **2016**, *120*, 1077-1082; b) S. Kumar, M. A. Isaacs, R. Trofimovaite, L. Durndell, C. M. Parlett, R. E. Douthwaite, B. Coulson, M. C. Cockett, K. Wilson, A. F. Lee, *Appl. Catal. B* **2017**, *209*, 394-404.

[40] G. QingáLu, *Chem. Commun.* **2009**, 3452-3454.

[41] D. Vione, T. Picatonotto, M. E. Carlotti, *J. Cosmet. Sci.* **2003**, *54*, 513-524.

[42] N. Barbero, D. Vione, *Environ. Sci. Technol.* **2016**, *50*, 2130.

[43] a) W. Yin, W. Wang, S. Sun, *Catal. Commun.* **2010**, *11*, 647-650; b) R.-C. Wang, C.-W. Yu, *Ultrason. Sonochem.* **2013**, *20*, 553-564; c) Y. Niu, M. Xing, J. Zhang, B. Tian, *Catal. Today* **2013**, *201*, 159-166; d) W. Shi, N. Chopra, *ACS Applied Materials & Interfaces* **2012**, *4*, 5590-5607; e) Y. Chen, W. Huang, D. He, Y. Situ, H. Huang, *ACS Appl. Mater. Interfaces* **2014**, *6*, 14405-14414.

[44] B. Tryba, A. W. Morawski, M. Inagaki, M. Toyoda, *Appl. Catal. B* **2006**, *63*, 215-221.

[45] a) M. Y. Moridani, A. Siraki, P. J. O'Brien, *Chem.-Biol. Interact.* **2003**, *145*, 213-223; b) J. Michalowicz, W. Duda, *Pol. J. Environ. Stud.* **2007**, *16*, 347-362.

[46] B. Sun, A. V. Vorontsov, P. G. Smirniotis, *Langmuir* **2003**, *19*, 3151-3156.

[47] a) C. G. Silva, J. L. Faria, *J. Mol. Catal. A* **2009**, *305*, 147-154; b) O. Gimeno, M. Carbajo, F. J. Beltrán, F. J. Rivas, *J. Hazard Mater.* **2005**, *119*, 99-108.

[48] a) B. Naik, K. Parida, G. Behera, *ChemCatChem* **2011**, *3*, 311-318; b) E. Grabowska, J. Reszczyńska, A. Zaleska, *Water Res.* **2012**, *46*, 5453-5471.

[49] C. Chen, W. Ma, J. Zhao, *Chem. Soc. Rev.* **2010**, *39*, 4206-4219.

[50] H. Park, H.-i. Kim, G.-h. Moon, W. Choi, *Energy Environ. Sci.* **2016**, *9*, 411-433.

[51] Y. Kwon, A. Soon, H. Han, H. Lee, *J. Mater. Chem. A* **2015**, *3*, 156-162.

[52] D. Barreca, P. Fornasiero, A. Gasparotto, V. Gombac, C. Maccato, T. Montini, E. Tondello, *ChemSusChem* **2009**, *2*, 230-233.

[53] J. Kondo, *Chem. Commun.* **1998**, 357-358.

[54] Z. Jiang, Z. Zhang, W. Shangguan, M. A. Isaacs, L. J. Durndell, C. M. A. Parlett, A. F. Lee, *Catal. Sci. Technol.* **2016**, *6*, 81-88.

[55] a) T. Maschmeyer, M. Che, *Angew. Chem.* **2010**, *122*, 1578-1582; b) T. Maschmeyer, M. Che, *Angew. Chem. Int-.Ed.* **2010**, *49*, 9590-9591.

[56] H. Kisch, *Angew. Chem. Int-.Ed.* **2010**, *49*, 9588-9589.

FULL PAPER

Entry for the Table of Contents

FULL PAPER